







RESEARCH ARTICLE | MAY 16 2024

The effect of grain boundaries and precipitates on the mechanical behavior of the refractory compositionally complex alloy NbMoCrTiAl

Jin Wang  ; Silva Basu; Alexander Kauffmann ; Martin Heilmaier ; Ruth Schwaiger  

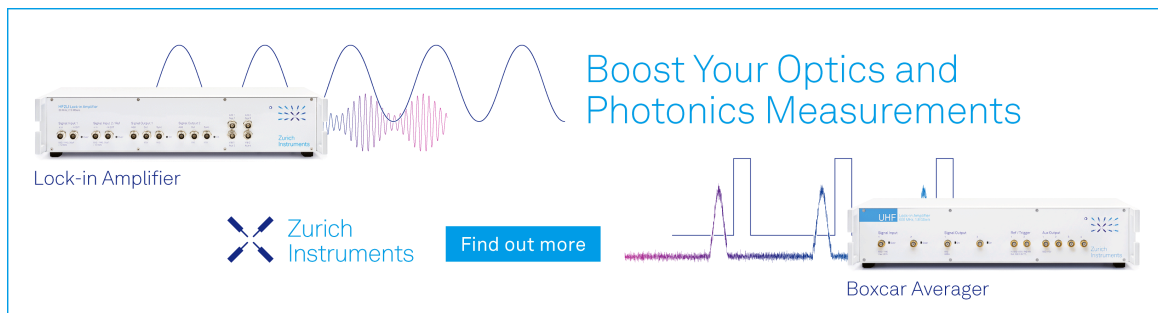
 Check for updates

Appl. Phys. Lett. 124, 201905 (2024)


<https://doi.org/10.1063/5.0203536>



Boost Your Optics and Photonics Measurements



Lock-in Amplifier



[Find out more](#)

Boxcar Averager

The effect of grain boundaries and precipitates on the mechanical behavior of the refractory compositionally complex alloy NbMoCrTiAl

Cite as: Appl. Phys. Lett. **124**, 201905 (2024); doi: [10.1063/5.0203536](https://doi.org/10.1063/5.0203536)

Submitted: 14 February 2024 · Accepted: 4 May 2024 ·

Published Online: 16 May 2024



View Online



Export Citation



CrossMark

Jin Wang,^{1,a)}  Silva Basu,¹ Alexander Kauffmann,²  Martin Heilmaier,²  and Ruth Schwaiger^{1,3,a)} 

AFFILIATIONS

¹Institute of Energy and Climate Research, Forschungszentrum Juelich GmbH, 52425 Juelich, Germany

²Institute for Applied Materials, Karlsruhe Institute of Technology (KIT), Engelbert-Arnold-Str. 4, 76131 Karlsruhe, Germany

³Chair of Energy Engineering Materials, Faculty 5, RWTH Aachen University, 52056 Aachen, Germany

Note: This paper is part of the APL Special Collection on Era of Entropy: Synthesis, Structure, Properties, and Applications of High Entropy Materials.

^{a)}Authors to whom correspondence should be addressed: jin.wang@fz-juelich.de and r.schwaiger@fz-juelich.de

ABSTRACT

Refractory compositionally complex alloys (CCAs) have been found to exhibit promising high-temperature properties. However, the brittleness of most CCAs at room temperature limits their application. To understand the influence of microstructure on the deformation behavior of these alloys, we conducted micromechanical experiments, including nanoindentation and micropillar compression tests, on a representative NbMoCrTiAl alloy at room temperature. The indentation at the grain boundaries showed increased shear stress and hardness compared to the matrix (ordered B2 crystal structure) due to the presence of local intermetallic precipitates (C14 and A15 phases). Although the NbMoCrTiAl alloy exhibits no ductility at the millimeter scale as shown in previous studies, the micropillars at the grain boundaries, which were decorated with precipitates, demonstrated higher yield strength and significant plastic strain >30% at room temperature. Numerous slip lines were observed, while cracks and fracture occurred at higher levels of deformation. The grain boundaries with precipitates increased the probability of crack initiation and propagation, but they did not necessarily lead to catastrophic failure of the pillars.

© 2024 Author(s). All article content, except where otherwise noted, is licensed under a Creative Commons Attribution (CC BY) license (<https://creativecommons.org/licenses/by/4.0/>). <https://doi.org/10.1063/5.0203536>

The concept of high entropy alloys (HEAs) and compositionally complex alloys (CCAs) was introduced as a metallurgical strategy to create materials with advanced properties for multifunctional applications.^{1,2} Compared to conventional alloys, HEAs and CCAs provide a broader range of selection and combinations of alloying elements, thus offering flexible alloy design to meet critical capabilities.^{2–6}

One promising approach to designing improved alloys for high-temperature applications, such as strength and corrosion and oxidation resistance, involves alloying different refractory elements to achieve higher solidus temperatures. A refractory CCA (RCCA) with high melting point consisting of five principal elements, i.e., the NbMoCrTiAl alloy, was designed for this purpose, aiming to improve mechanical behavior, such as yield strength and ultimate strength at elevated temperatures.^{7,8} However, RCCAs often lack ductility at room temperature.² For instance, compression experiments at the millimeter scale showed a lack of plasticity of the NbMoCrTiAl alloy below a

temperature of 400 °C.⁷ The brittleness of the NbMoCrTiAl alloy at room temperature was rationalized with its ordered B2 crystal structure³ and the presence of intermetallic grain boundary precipitates.⁹ Nevertheless, these previous studies and experiments were conducted on polycrystalline samples; thus, the results have to be considered as the interplay of all microstructural features. Recently, notable plastic deformation of single-crystalline NbMoCrTiAl at room temperature together with numerous slip lines was observed in micro-cantilevers and micropillars.¹⁰ This suggests that the grain boundaries decorated with precipitates could be critical for the brittle behavior of the NbMoCrTiAl alloy, and the local deformation behavior needs to be characterized.

A NbMoCrTiAl sample (cast and homogenized at 1573 K for 20 h) cold-mounted, ground with SiC papers, and then gently polished using an OP-A (acidic alumina) suspension of 0.05 μm grain size was investigated. Details of the procedures to produce the material can be found elsewhere.^{7,8} The microstructure was characterized using

electron backscatter diffraction (EBSD) (AZtecHKL, Oxford Instruments, UK) and energy dispersive x-ray spectroscopy (EDS) (X-Max Extreme, Oxford Instruments, UK) analyses in a scanning electron microscope (SEM) (Merlin Gemini-2, Zeiss, Germany). Micropillars were prepared at selected grain boundaries using focused ion beam (FIB) milling (Auriga, Zeiss, Germany). After FIB preparation, the geometry and distribution of the precipitates in each pillar were characterized by SEM for further analysis, such as determining the stress vs strain and the fracture behavior. The pillars were $\sim 10 \mu\text{m}$ in height with an aspect ratio of $\sim 3:1$ (height-to-diameter). The pillar diameter was kept in the range of $\sim 3\text{--}5 \mu\text{m}$ to avoid significant size-dependent ductility observed for smaller pillar diameters.^{11,12} Micromechanical experiments, including nanoindentation and micro-compression tests, were conducted using a standard nanoindenter (Nano Indenter XP, MTS Systems Corp., Eden Prairie, MN, US) with a diamond Berkovich tip and a diamond flat-ended punch (of $10 \mu\text{m}$ diameter), respectively. For comparison, indentation experiments were also performed in TaNbHfZrTi, which is a BCC refractory HEA with excellent room temperature ductility.¹³

Nanoindentation experiments were performed in different grains and precipitates at constant loading rate (CLR) and constant strain rate (CSR) using continuous stiffness measurement (CSM). After nanoindentation, EBSD and EDS analyses were employed to determine the orientation and phase of the indented area. Consequently, the mechanical behavior of each indent was correlated with the microstructure, as shown in Fig. 1.

Figure 1(a) shows the load–displacement (P – h) behavior of 79 indents at a loading rate of 0.01 mN/s to a load of 1 mN . Clear pop-ins are observed in the curves, which are related to the dislocation nucleation mechanism and mark the transition from elastic to elastic–plastic deformation during the loading process.¹⁴ Before the pop-in, the P – h curve can be described by the Hertzian contact relation,¹⁵ as indicated by the dashed line in Fig. 1(a). An array of indents with a spacing of $4 \mu\text{m}$ [Fig. 1(b)] was made over an area of three grains and the grain

boundaries in-between. The crystal orientation does not have a significant effect on the P – h behavior [Fig. 1(a)]. EBSD and EDS were used to characterize the grain orientations and phases present in the NbMoCrTiAl sample. The matrix of NbMoCrTiAl is known to be B2-structured,³ which, though, cannot be identified by EBSD. The precipitates were identified by EBSD phase map as C14 structured Laves phase (EDS showing enriched in Nb and Cr) and A15 phase (enriched in Nb and Al) localized at the grain boundaries and the triple point. At the grain boundary, in addition a Ti-rich BCC phase is observed tagged by the arrow in Fig. 1(c). Indentation at the grain boundaries and of the precipitates results in quite distinct curves, as indicated by the arrows and circles in Figs. 1(a) and 1(b). Compared to the indents in the B2 matrix, indentation of the precipitates suggests relatively higher pop-in loads (P^* , at which the pop-in starts) and the corresponding loading curves are steeper than those of the matrix.

The pop-in load P^* determined from the CLR experiments was used to calculate the maximum shear stress τ_{max} according to Refs. 15–17,

$$\tau_{\text{max}} = 0.31P_m = 0.31 \left(\frac{6E_r^2}{\pi^3 R^2} P^* \right)^{\frac{1}{3}}, \quad (1)$$

with P_m being the maximum pressure, E_r the reduced modulus determined from nanoindentation,¹⁸ and R the tip radius determined by a Hertzian fit¹⁵ [Fig. 1(a)]. With a dataset of ~ 100 indents, τ_{max} was statistically analyzed to estimate the activation volume V_y^* related to the dislocation nucleation in the material.^{19–21} The cumulative distribution function (CDF) f of the shear stress τ can be described as

$$f = 1 - \exp \left[- \frac{N_0 k T}{\dot{\epsilon} V_y^*} \cdot \exp \left(- \frac{\epsilon}{k T} \right) \cdot \left(\frac{\tau V_y^*}{k T} \right) \right], \quad (2)$$

and

$$\ln [-\ln (1 - f)] = \ln \frac{N_0 k T}{\dot{\epsilon} V_y^*} - \frac{\epsilon}{k T} + \frac{\tau V_y^*}{k T}, \quad (3)$$

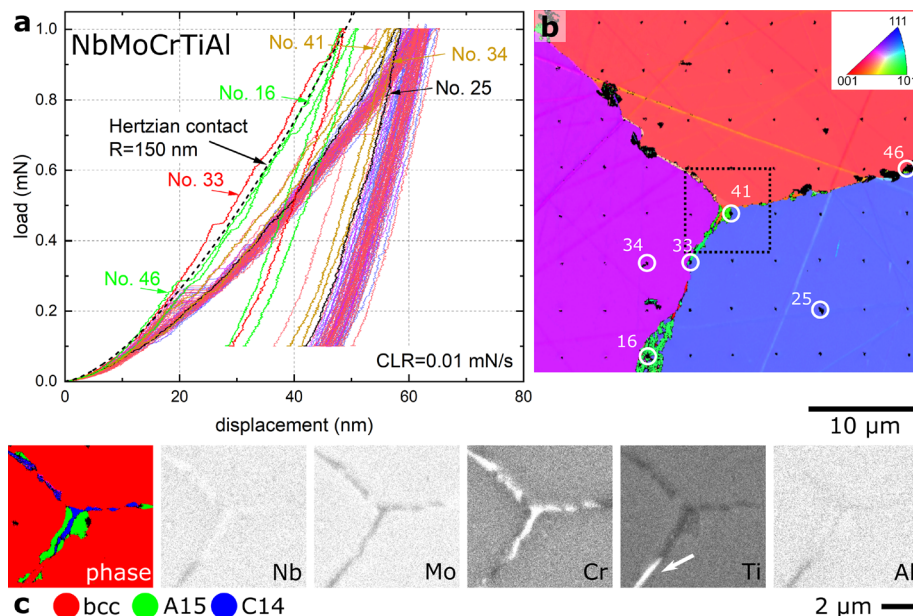


FIG. 1. The nanoindentation load–displacement (P – h) curves reflect the microstructure of the NbMoCrTiAl sample: (a) P – h curves of 79 indents at a constant loading rate (CLR) of 0.01 mN/s exhibit significant scatter. (b) The inverse pole figure (IPF) shows the out-of-plane orientation of every indent position. The colors of the curves in (a) were selected according to the crystal orientations and the IPF in (b). The indents at the grain boundaries and precipitates are marked by numbers and circles in (a) and (b). (c) The phase map and composition maps of the area indicated in (b) reveal precipitates at the grain boundaries and at the triple point.

with N_0 as the constant frequency describing the probability of dislocation nucleation, ε the intrinsic nucleation energy barrier, that is, the activation energy, and k and T the Boltzmann constant and temperature, respectively. Under the CLR condition, the stress rate $\dot{\tau}$ is constant. Different microstructural features of NbMoCrTiAl and TaNbHfZrTi were characterized by CLR nanoindentation tests; different grains as well as regions with grain boundaries were indented. In previous studies, intermetallic phases were found in NbMoCrTiAl,^{9,10} while TaNbHfZrTi consists of a single disordered BCC phase (A2).^{10,13} Two loading rates, 0.005 mN/s and 0.01 mN/s, were applied. In Fig. 2, the calculated τ_{\max} values from CLR nanoindentation tests are plotted according to Eqs. (2) and (3).

The τ_{\max} values of NbMoCrTiAl determined from the experiments shown in Fig. 1 are plotted as the black symbols in Fig. 2 and exhibit the broadest scattering among all datasets. This can be attributed to the presence of complex intermetallic phases at the grain boundaries. For comparison, another indentation array of ~ 100 indents was performed in the same area, but with an increased spacing of $15 \mu\text{m}$ to avoid the grain boundaries and precipitates. The τ_{\max} values are shown as red symbols in Fig. 2. The scatter is significantly reduced, and all data are less than the theoretical shear strength (defined as $G/2\pi$, where G is the shear modulus). The cumulative distribution, however, exhibits a discontinuous shape compared to the distribution of the τ_{\max} values obtained from one grain (gray symbols in Fig. 2). The two distributions overlap partially, but the distribution of τ_{\max} values determined in one grain is sharp and continuous as also seen in the $\ln[-\ln(1-f)]-\tau_{\max}$ plot in Fig. 2(b). The discontinuous distribution of τ_{\max} in different grains is likely related to the orientation-related shear stress²² due to the ordered B2 matrix,^{3,9,10} since the number of available slip system is limited. The dataset determined for the TaNbHfZrTi sample (blue symbols in Fig. 2) does not exhibit grain boundary- and orientation-related behavior.

According to Eq. (3), the slope of the $\ln[-\ln(1-f)]-\tau_{\max}$ behavior [Fig. 2(b)] provides the value of V_y^*/kT under the CLR condition. For the TaNbHfZrTi and NbMoCrTiAl alloys, V_y^* is determined and normalized to the respective lattice parameters (0.340 nm for

TaNbHfZrTi¹³ and 0.315 nm for NbMoCrTiAl⁸), yielding $\sim 1 \Omega$ and $\sim 2 \Omega$, respectively. For the NbMoCrTiAl alloy, the slope of data from one grain is used to eliminate the scatter induced by precipitates and different crystal orientations. The normalized V_y^* values suggest^{20,23} that dislocation nucleation in TaNbHfZrTi is attributed to point-like defects, while nucleation in NbMoCrTiAl involves more than one atom, which complicates the process and, therefore, makes dislocation nucleation more difficult than in the TaNbHfZrTi alloy or other conventional BCC metals.

The elastic modulus and hardness of different grains in NbMoCrTiAl and precipitates at grain boundaries were characterized by CSR nanoindentation tests, with the results shown in Fig. 3.

At an indentation strain rate of 0.05 s^{-1} , the elastic modulus and hardness were determined continuously to a depth of $\sim 1800 \text{ nm}$. The elastic modulus of 12 grains yields an average value of $196.7 \pm 0.9 \text{ GPa}$ and is constant over the depth, while the hardness exhibits a pronounced indentation size effect.²⁴ Fitting $H-h$ for $h > 400 \text{ nm}$ by applying the Nix-Gao model,²⁴ the depth-independent hardness H_0 was determined as $7.02 \pm 0.17 \text{ GPa}$. Generally, the elastic modulus and hardness determined for one out-of-plane orientation tend to group closely, while also the overall variation is small. In some cases, hardness behaviors significantly different from those found in the majority of tests were observed. Lower hardness values were found to be caused by pre-existing pores in the sample, while higher hardness was due to precipitates decorating the grain boundaries (b and c in Fig. 3). SEM images in Figs. 3(b) and 3(c) show that the two types of precipitates [C14 and A15 phases, confirmed by EBSD analysis in Fig. 1(c)] at the grain boundaries contribute to higher hardness, while a crack was also observed at one corner of an indent on a precipitate.

Nanoindentation was used to determine the mechanical properties that reflect the microstructure around and below the indentation. To evaluate the effect of the subsurface microstructure, micropillars were prepared at selected grain boundaries, specifically at three grain boundaries between $\{100\}$ and $\{110\}$ grains denoted as GB1, GB2, and GB3 (Fig. 4), to include the precipitates along the longitudinal axis of the pillar. Depending on the length of the grain boundaries, one to

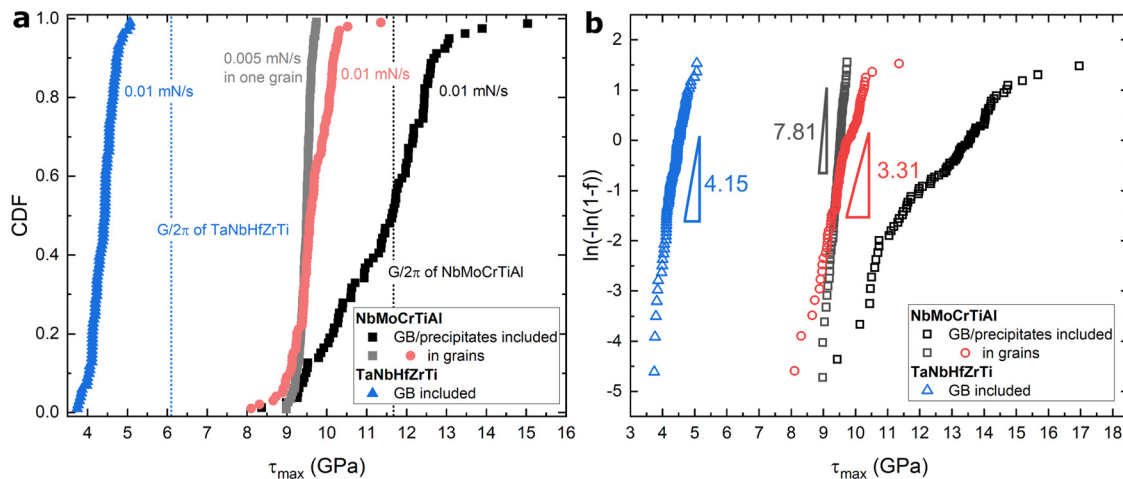


FIG. 2. Maximum shear stress values τ_{\max} determined from CLR experiments are shown in the cumulative probability distribution. (a) The cumulative distribution function (CDF) of τ_{\max} of the NbMoCrTiAl alloy is compared to the TaNbHfZrTi alloy. The theoretical shear strength of each RCCA is marked by the dashed lines. (b) The $\ln[-\ln(1-f)]-\tau_{\max}$ plot gives a slope to determine the activation volume for the individual case.

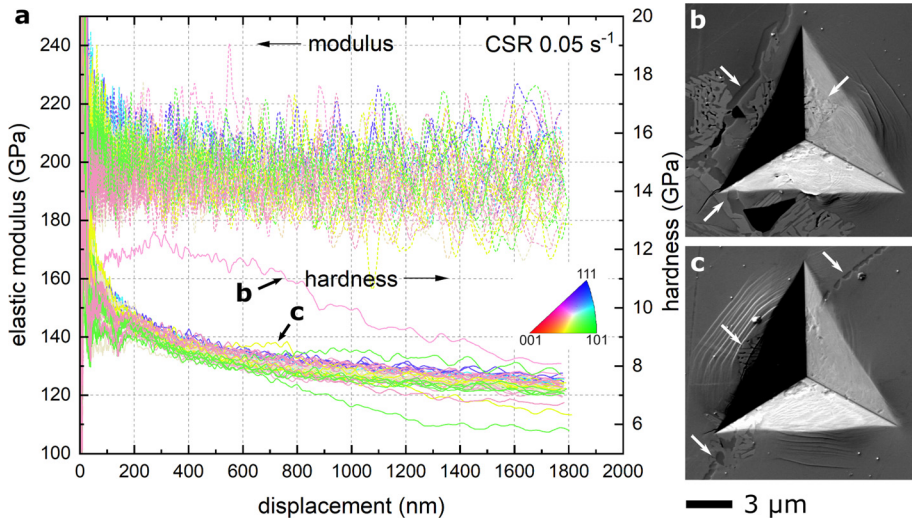


FIG. 3. 50 indents covering 12 grains show the mechanical response of the grains and at the grain boundaries. (a) Elastic modulus (E) and hardness (H) were determined continuously over the indentation depth (h) at a constant strain rate of 0.05 s^{-1} . The colors of the curves correspond to the crystalline orientation referring to the IPF triangle in the inset. A significant increase in hardness is observed in some tests, for example, marked by **b** and **c**. The corresponding indents are found at grain boundaries with precipitates (arrows) shown in SEM images in (b) and (c).

three pillars were prepared at each grain boundary. The uneven distribution of precipitates at the grain boundaries resulted in varying local ratios of precipitates in each pillar (Fig. S1). Prior to the compression experiment, SEM was used to determine the distribution of precipitates, grain boundary path, and pillar geometry. The P-h response was then converted into stress vs strain behavior.^{10,25} The micro-compression experiments were conducted at a constant displacement rate of 20 nm/s corresponding to the strain rate of $\sim 2 \times 10^{-3} \text{ s}^{-1}$.

All pillars exhibited a yield point and sustained strains of $\sim 35\%$, as shown in the stress-strain behavior in Fig. 4(a). Such a high level of plasticity of micropillars in this size regime is unexpected compared to many micropillar experiments of brittle materials,^{26–28} which typically reported strains $< 10\%$, as NbMoCrTiAl showed brittle behavior in millimeter-scale compression tests;⁷ brittle intermetallic precipitates at

the grain boundaries were considered the main cause for brittle fracture. Yet, in this study, the pillars at the grain boundaries show higher yield strength compared to the single-crystalline pillars of similar geometry and orientation¹⁰ [gray band in Fig. 4(a) shows the yield strength range of $\langle 100 \rangle$ and $\langle 110 \rangle$ loading directions in single-crystalline pillars]. In some pillars, such as P_{1-1} , P_{3-1} , and P_{3-2} (with the indices referring to grain boundary and pillar number), a continuous increase in stress with increasing strain was observed. In general, the stress vs strain behaviors did not reveal a strong dependence on the type of grain boundaries, that is, the orientation of the neighboring grains. Rather, the distribution of precipitates played a major role and affected the mechanical behavior.

The SEM images [Figs. 4(b)–4(d)] confirm the presence of slip lines on the surfaces after compression, indicating plastic deformation.

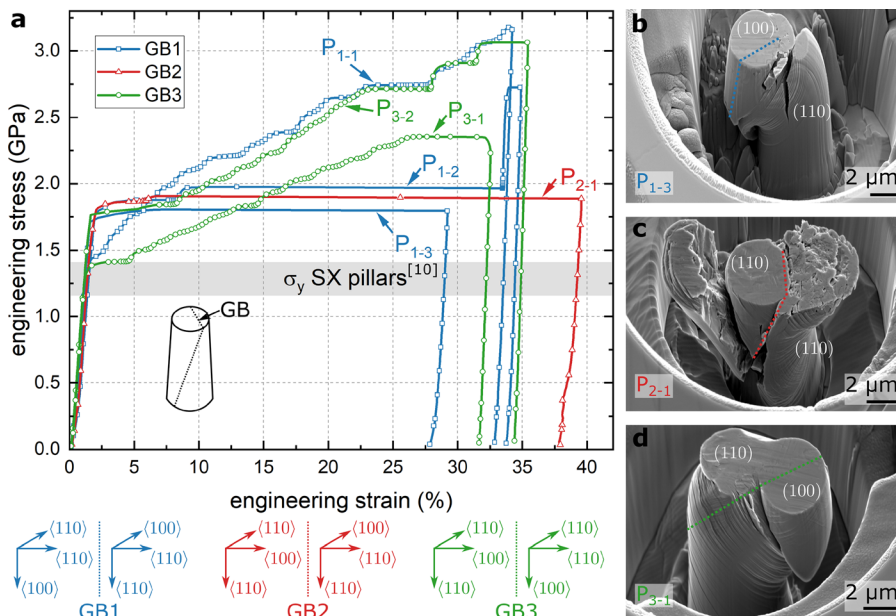


FIG. 4. Stress vs strain behavior of micropillars at grain boundaries in NbMoCrTiAl. (a) Stress-strain curves of pillars prepared at three grain boundaries between $\{100\}$ and $\{110\}$ grains indicated as GB1, GB2, and GB3. The gray band marks the range of yield strength of single-crystalline (SX) pillars of comparable geometry and orientations.¹⁰ The pillars are denoted as $P_{\text{GB-pillar}}$. (b)–(d) SEM images show the compressed pillars at the three grain boundaries, and the grain boundaries are marked by the dashed lines.

16 May 2024 12:43:32

The grains exhibit parallel slip lines that terminate at the grain boundary decorated with precipitates. The width of the precipitate band varies from several tens of nm to $\sim 1 \mu\text{m}$, depending on the local amount of precipitates (Fig. S1). The presence of precipitates in a grain inhibits the movement of dislocations and slip lines across the grain boundary, resulting in a slip-line-free zone. This band of precipitates, thus, provides additional strengthening to the pillar until a crack initiates. Fracture of the pillars typically occurs at the boundaries between the precipitates and the B2 matrix, along which cracks grow and merge. The pillar P_{3-1} [Fig. 4(d)] represents an exception. Its precipitate row is relatively thin, which allows the slip lines to pass through. As a result, the stress-strain behavior is similar to that of a single-crystalline pillar, and the yield strength is comparable to the upper limit of the values obtained from the compression of a single-crystalline pillar.

In summary, micromechanical experiments, including nanoindentation and micropillar compression tests, were performed on the RCCA NbMoCrTiAl. Our study focused on the effect of precipitates, such as the C14 and A15 phases, on the mechanical behavior. Overall, the micropillars containing grain boundaries decorated with precipitates demonstrate the unique characteristics and behavior of the RCCA NbMoCrTiAl at the microscale. The NbMoCrTiAl matrix has an activation volume V_y^* twice that of BCC (A2 structure) TaNbHfZrTi, indicating a greater number of atoms involved in the dislocation nucleation process. This explains the distinct plastic behaviors observed for the two RCCAs. The nanoindentation tests demonstrate that the precipitates exhibit higher shear strength and hardness. The pillars with precipitates exhibit higher yield strength in stress-strain behavior compared to single-crystalline pillars. Despite the increased probability for cracks due to the precipitates, plastic deformation and slip lines were observed in all grain boundary pillars. At higher levels of deformation, cracks were observed, but they did not result in catastrophic failure of all pillars. Slip lines were also observed to cross grain boundaries with precipitates that were arranged in rather thin lines, indicating that careful tuning of the shape, distribution, and fraction of precipitates can introduce them as a strengthening phase into the matrix without significantly sacrificing plasticity.

See the [supplementary material](#) for details: Fig. S1 presents SEM images of the micropillars P_{1-3} , P_{2-1} , and P_{3-1} showing the distribution of precipitates (from the side and top). (a) The side and top (inset) view of pillars before the compression experiments. Two kinds of precipitates, A15 (marked by black arrows) and C14 (white arrows), were observed along the grain boundary. The tilt angle of 40° was corrected. (b) Precipitates were identified after the compression experiments. Compared to the other pillars [also P_{2-1} shown in Fig. 4(c)], the line of precipitates in P_{3-1} is thinner and no significant cracks were observed after the compression experiment in this pillar.

This research was financially supported by the Deutsche Forschungsgemeinschaft (DFG), Grant No. SCHW855/6-1, within the Priority Program SPP2006 “Compositionally Complex Alloys—High Entropy Alloys (CCA-HEA).” The sample preparation and characterization were supported by Mr. Gutzeit, Dr. Grüner, and Dr. Wessel from IEK-2.

AUTHOR DECLARATIONS

Conflict of Interest

The authors have no conflicts to disclose.

Author Contributions

Jin Wang: Conceptualization (equal); Data curation (equal); Formal analysis (equal); Methodology (equal); Visualization (equal); Writing – original draft (equal); Writing – review & editing (equal). **Silva Basu:** Data curation (equal); Formal analysis (equal); Investigation (equal). **Alexander Kauffmann:** Resources (lead); Writing – review & editing (supporting). **Martin Heilmaier:** Resources (lead); Writing – review & editing (supporting). **Ruth Schwaiger:** Conceptualization (equal); Funding acquisition (equal); Methodology (equal); Project administration (equal); Resources (equal); Supervision (equal); Writing – original draft (equal); Writing – review & editing (equal).

DATA AVAILABILITY

The data that support the findings of this study are available from the corresponding authors upon reasonable request.

REFERENCES

1. W. Yeh, S.-K. Chen, S.-J. Lin, J.-Y. Gan, T.-S. Chin, T.-T. Shun, C.-H. Tsau, and S.-Y. Chang, “Nanostructured high-entropy alloys with multiple principal elements: Novel alloy design concepts and outcomes,” *Adv. Eng. Mater.* **6**(5), 299–303 (2004).
2. E. P. George, D. Raabe, and R. O. Ritchie, “High-entropy alloys,” *Nat. Rev. Mater.* **4**(8), 515–534 (2019).
3. H. Chen, A. Kauffmann, S. Seils, T. Boll, C. Liebscher, I. Harding, K. S. Kumar, D. V. Szabó, S. Schlabach, S. Kauffmann-Weiss *et al.*, “Crystallographic ordering in a series of Al-containing refractory high entropy alloys Ta–Nb–Mo–Cr–Ti–Al,” *Acta Mater.* **176**, 123–133 (2019).
4. D. B. Miracle and O. N. Senkov, “A critical review of high entropy alloys and related concepts,” *Acta Mater.* **122**, 448–511 (2017).
5. F. Liu, P. K. Liaw, and Y. Zhang, “Recent progress with BCC-structured high-entropy alloys,” *Metals* **12**(3), 501 (2022).
6. M.-H. Tsai and J.-W. Yeh, “High-entropy alloys: A critical review,” *Mater. Res. Lett.* **2**(3), 107–123 (2014).
7. H. Chen, A. Kauffmann, B. Gorr, D. Schliephake, C. Seemüller, J. Wagner, H.-J. Christ, and M. Heilmaier, “Microstructure and mechanical properties at elevated temperatures of a new Al-containing refractory high-entropy alloy Nb–Mo–Cr–Ti–Al,” *J. Alloys Compd.* **661**, 206–215 (2016).
8. H. Chen, A. Kauffmann, S. Laube, I.-C. Choi, R. Schwaiger, Y. Huang, K. Lichtenberg, F. Müller, B. Gorr, H.-J. Christ *et al.*, “Contribution of lattice distortion to solid solution strengthening in a series of refractory high entropy alloys,” *Metall. Mater. Trans. A* **49**, 772–781 (2018).
9. F. Müller, B. Gorr, H.-J. Christ, H. Chen, A. Kauffmann, S. Laube, and M. Heilmaier, “Formation of complex intermetallic phases in novel refractory high-entropy alloys NbMoCrTiAl and TaMoCrTiAl: Thermodynamic assessment and experimental validation,” *J. Alloys Compd.* **842**, 155726 (2020).
10. J. Wang, N. J. Peter, M. Heilmaier, and R. Schwaiger, “Plasticity of the TaNbHfZrTi and NbMoCrTiAl refractory compositionally complex alloys at room temperature,” submitted (2024).
11. W. W. Gerberich, J. Michler, W. M. Mook, R. Ghisleni, F. Östlund, D. D. Stauffer, and R. Ballarini, “Scale effects for strength, ductility, and toughness in “brittle” materials,” *J. Mater. Res.* **24**(3), 898–906 (2009).
12. P. R. Howie, S. Korte, and W. J. Clegg, “Fracture modes in micropillar compression of brittle crystals,” *J. Mater. Res.* **27**(1), 141–151 (2012).
13. O. N. Senkov, J. M. Scott, S. V. Senkova, D. B. Miracle, and C. F. Woodward, “Microstructure and room temperature properties of a high-entropy TaNbHfZrTi alloy,” *J. Alloys Compd.* **509**(20), 6043–6048 (2011).

- ¹⁴T. F. Page, W. C. Oliver, and C. J. McHargue, "The deformation behavior of ceramic crystals subjected to very low load (nano)indentations," *J. Mater. Res.* **7**(2), 450–473 (1992).
- ¹⁵K. L. Johnson and K. L. Johnson, *Contact Mechanics* (Cambridge University Press, Cambridge, United Kingdom, 1987).
- ¹⁶R. W. K. Honeycombe, *The Plastic Deformation of Metals*, 2nd ed. (Arnold, London, 1985). ISBN: 0713134682
- ¹⁷D. F. Bahr, D. E. Kramer, and W. W. Gerberich, "Non-linear deformation mechanisms during nanoindentation," *Acta Mater.* **46**, 3605–3617 (1998).
- ¹⁸W. C. Oliver and G. M. Pharr, "An improved technique for determining hardness and elastic modulus using load and displacement sensing indentation experiments," *J. Mater. Res.* **7**(6), 1564–1583 (1992).
- ¹⁹C. A. Schuh and A. C. Lund, "Application of nucleation theory to the rate dependence of incipient plasticity during nanoindentation," *J. Mater. Res.* **19**(7), 2152–2158 (2004).
- ²⁰C. A. Schuh, J. K. Mason, and A. C. Lund, "Quantitative insight into dislocation nucleation from high-temperature nanoindentation experiments," *Nat. Mater.* **4**(8), 617–621 (2005).
- ²¹J. K. Mason, A. C. Lund, and C. A. Schuh, "Determining the activation energy and volume for the onset of plasticity during nanoindentation," *Phys. Rev. B* **73**(5), 054102 (2006).
- ²²T. L. Li, Y. F. Gao, H. Bei, and E. P. George, "Indentation Schmid factor and orientation dependence of nanoindentation pop-in behavior of NiAl single crystals," *J. Mech. Phys. Solids* **59**(6), 1147–1162 (2011).
- ²³J. Hirth and J. Lothe, *Theory of Dislocations* (Wiley, 1982).
- ²⁴W. D. Nix and H. Gao, "Indentation size effects in crystalline materials: A law for strain gradient plasticity," *J. Mech. Phys. Solids* **46**(3), 411–425 (1998).
- ²⁵S. Weyand, "Mikromechanische Charakterisierung multifunktionaler NIPU-Materialien und NIPU-(Nano)Komposite," Ph.D. thesis [KIT-Bibliothek, Karlsruher Institut für Technologie (KIT), Karlsruhe, 2020].
- ²⁶L. Jiang and N. Chawla, "Mechanical properties of Cu₆Sn₅ intermetallic by micropillar compression testing," *Scr. Mater.* **63**(5), 480–483 (2010).
- ²⁷W. Chen, Z. Huang, S. Cao, Y. Pan, M. Huang, Q. Hu, D. Xu, Q. Sun, L. Xiao, and J. Sun, "Strain rate-induced plasticity in bcc β -Ti alloy single crystal micropillars containing brittle ω -precipitates," *Mater. Des.* **137**, 404–413 (2018).
- ²⁸N. Takata, H. Ghassemi Armaki, Y. Terada, M. Takeyama, and K. S. Kumar, "Plastic deformation of the C14 Laves phase (Fe,Ni)₂Nb," *Scr. Mater.* **68**, 615–618 (2013).